Multiple heteroatom-doped urea and thiourea-derived polymeric carbon nitride for high-performance visible light-driven photocatalytic O_2 reduction to H_2O_2

Sitan Li [a], Bo Feng [a], Xiaoxin Zhang [b], Jing Tian [a], Dan Wang [a], Yan Pei [a], Minghua Qiao [a,*], Yefei Li [a,*], Baoning Zong [b,*]

[a] *Collaborative Innovation Center of Chemistry for Energy Materials, Department of Chemistry and Shanghai Key Laboratory of Molecular Catalysis and Innovative Materials, Fudan University, Shanghai 200438, PR China*
[b] *State Key Laboratory of Catalytic Materials and Chemical Engineering, Research Institute of Petroleum Processing, SINOPEC, Beijing 100083, PR China*

ARTICLE INFO

ABSTRACT

To photocatalytically reduce O_2 to H_2O_2 over polymeric carbon nitride (PCN) in high efficiency is essential for practical application but remains a considerable challenge. Herein, we synthesized a K, S, and O co-doped PCN (*akut*-CN) via one-pot polymerization of urea and thiourea in the presence of KCl and NaOH, which afforded an unprecedentedly high H_2O_2 production rate of 4.46 mM h^{-1} under visible light irradiation, about 210 times that over the un-doped PCN. The heteroatom doping and the incorporation of the cyano and hydroxyl groups into *akut*-CN are identified to enhance light absorption, accelerate the separation and transfer of the photogenerated charges, and improve the surface electronegativity and the O_2 adsorption capacity and strength, which collaboratively boosted the reaction kinetics. This work highlights the great potential of the elaborately decorated PCN in photocatalytic O_2 reduction to H_2O_2 and paves the way to the decentralized production and application of H_2O_2.

1. Introduction

Hydrogen peroxide (H_2O_2) is an eco-friendly oxidant widely used for organic synthesis, disinfection, wastewater treatment, pulp and paper bleaching, Fenton reaction, promising new high-energy liquid fuel, and so on [1,2]. The content of active oxygen in H_2O_2 is as high as 47.1 wt%, and only the non-toxic H_2O and O_2 byproducts are resulted after reaction. Currently, more than 95 % of the market share of H_2O_2 is produced by the anthraquinone (AQ) process. The AQ process mainly involves the hydrogenation of the alkyl-substituted anthraquinones with H_2 on a Ni or Pd catalyst, followed by the oxidation of anthrahydroquinones with O_2. Since this process requires high energy input and generates a lot of wastewater and solid wastes, the synthesis of H_2O_2 directly for the reaction between H_2 and O_2 in the presence of Pd or Pd-based bimetallic catalysts has been put forward [3–6]. However, for the time being, this process confronts a dilemma that an active catalyst may add up to the explosion risk, while a mediocre catalyst will lead to poor production efficiency.

Artificial photosynthesis has received enormous attention, as it can transform sustainable solar energy into valuable chemicals. Driven by sunlight, photogenerated electrons on appropriate photocatalysts can selectively reduce O_2 to H_2O_2 via the proton-coupled two-electron mechanism (O_2 + 2H$^+$ + 2e$^-$ → H_2O_2, $E°$ = 0.68 V vs NHE) [2]. Compared with the AQ and H_2–O_2 direct synthesis processes, the photocatalytic reduction of O_2 is inherently economic, energy-saving, and safe. Among the catalysts investigated for this aim, the polymeric carbon nitride (PCN), with graphitic carbon nitride (*g*-C$_3$N$_4$) as a representative, is one of the most promising candidates, as its conduction band bottom (–1.3 V) is suitable for O_2 reduction to H_2O_2, while its valence band top (1.4 V) is higher than those of metal oxide semiconductor catalysts, rendering it lower activity towards the undesired oxidative decomposition of H_2O_2 [7–10]. Moreover, PCN only contains earth-abundant elements [11–14]. Unfortunately, PCN usually suffers from sluggish kinetics in photocatalytic O_2 reduction to H_2O_2 due to its low visible light harvesting ability, high recombination rate of the photogenerated electron–hole pairs, slow transfer of the charge carriers, limited active sites due to the small surface area, and low O_2 adsorption ability due to lacking in the surface functional groups. Hence, many strategies, such as

---

* Corresponding authors.
  E-mail addresses: mhqiao@fudan.edu.cn (M. Qiao), yefeil@fudan.edu.cn (Y. Li), zongbn.ripp@sinopec.com (B. Zong).

morphological control [15], heteroatom doping [7,16–19], surface vacancy engineering [20,21], heterostructure construction [22–25], and co-catalyst loading [26], have been proposed, among which heteroatom doping turns out to be highly flexible and effective in improving the H_2O_2 production kinetics over PCN. For example, Choi and co-workers reported that the in situ doped K, P, and O accelerated the interfacial electron transfer to O_2 while retarding H_2O_2 decomposition [16]. The incorporation of KPF_6 in forms of K^+ in the nitrogen pot and PF_6^- inside the PCN framework greatly improved the apparent quantum yield (AQY) and reaction specificity [17]. The synergistic effects of K bridging and S substitution promoted the interlayer charge separation and polarization of trapped electrons for oxygen capture and reduction [7]. Zhu and co-workers found that the O-enriched structures (–COOH and C–O–C) could enhance the activity and selectivity [21]. Lei and co-workers identified that the in situ grafted hydroxyl groups could capture the photogenerated holes to improve the availability of the electrons and protons and help in suppressing H_2O_2 decomposition [18]. On the other hand, He and co-workers found that the introduction of –NH–CH_2–OH did not change the charge separation and transfer properties, but markedly improved the O_2 adsorption property, thus benefiting the reduction kinetics of O_2 to H_2O_2 [19]. However, the efficiency of the PCN-based photocatalysts in photocatalytic O_2 reduction to H_2O_2 still needs further improvement to satisfy the demands of practical applications [1].

Herein, we fabricated a K, S, and O co-doped PCN (*akut*-CN) by one-pot polymerization of urea and thiourea in the presence of KCl and NaOH. In photocatalytic reduction of O_2 to H_2O_2, the multiple heteroatom-doped *akut*-CN displayed unprecedentedly high H_2O_2 production rate under visible light irradiation and excellent selectivity and stability. It is revealed that urea renders *akut*-CN with high specific surface area. KCl not only acts as the source of K, but also induces the formation of the cyano groups. NaOH further promotes the formation of the cyano groups and additionally incorporates the hydroxyl groups to the PCN framework. Photoelectric characterizations demonstrated that *akut*-CN possesses the highest concentration and separation and interface transfer efficiencies of the photoinduced charges. Moreover, *akut*-CN is the most negatively charged and displays the highest O_2 adsorption capacity and binding strength, which are collectively kinetically advantageous to the photocatalytic reduction of O_2 to H_2O_2 via the proton-coupled two-electron mechanism.

2. Experimental

2.1. Catalyst preparation

For the preparation of the *u*-CN material, 10 g of urea were placed in a 50 mL ceramic crucible with a cap, and then calcinated at 823 K for 4 h at a ramping rate of 2 K min^{-1} in a muffle furnace. The S-doped PCN (*ut*-CN) materials were similarly prepared except for using urea and thiourea mixed by grinding as the precursor. To screen out the optimal composition of *ut*-CN, the mass ratios of urea to thiourea of 7/1, 5/1, 3/1, and 1/1 were investigated.

The K,S-doped PCN (*kut*-CN) materials were prepared similarly to *ut*-CN except for mixing an appropriate amount of KCl with urea and thiourea by grinding prior to calcination at 723 K. Note that no material was left after washing with distilled water when calcinated at 823 K. To screen out the optimal composition of *kut*-CN, the mass ratios of KCl to urea and thiourea of 0.5/1, 1/1, 2/1, and 3/1 were investigated. The mass ratio of urea to thiourea was fixed at the optimal value of 5/1 obtained above.

The alkalized K,S-doped PCN (*akut*-CN) materials were prepared similarly to *kut*-CN except for by mixing a suitable amount of NaOH with KCl, urea, and thiourea by grinding prior to calcination at 823 K. To screen out the optimal composition of *akut*-CN, the mass ratios of NaOH to KCl, urea, and thiourea of 1/120, 1/80, 1/60, and 1/40 were investigated. The mass ratio of KCl to urea and thiourea was fixed at the

optimal value of 1/1 obtained above. For simplicity, *akut*-CN is used to represent the material prepared at the mass ratio of 1/60 and calcination temperature of 823 K if unspecified. The *akut*-CN-*T* materials were prepared by calcinating the *akut*-CN precursor at 723, 748, 773, and 798 K and denoted as *akut*-CN-723, *akut*-CN-748, *akut*-CN-773, and *akut*-CN-798, respectively.

After calcination, the as-synthesized CN materials were washed with distilled water and centrifuged at 8000 rpm for 9 times, while the alkalized materials were washed until the pH of the solution ~7. Then, the materials were dried at 353 K overnight before usage.

2.2. Photocatalytic testing and H_2O_2 quantification

The photocatalytic reduction of O_2 to H_2O_2 was carried out in a batch-wise stirred water-jacketed cylindrical glass reactor (height of 11 cm and inner diameter of 7 cm) fitted with a quartz cover (thickness of 0.8 cm and diameter of 11 cm) on top. In the reactor, 50 mg of the catalyst was dispersed in a solution containing 90 mL of H_2O and 10 mL of ethanol by ultrasonication for 5 min. Then, O_2 was bubbled into the solution at 30 mL min^{-1} for 30 min to expel the air in the solution and the reactor. After that, photoirradiation was turned on, and O_2 was bubbled at 10 mL min^{-1} throughout the reaction at the stirring rate of 400 rpm. A 300 W xenon lamp (CEL-HXF300; Beijing China Education Au-light Co., Ltd.) coupled with a UV-cutoff filter (420 nm $\leq \lambda \leq$ 780 nm) was employed as the light radiation source. The reactor was thermostated at 298 $\pm$ 5 K by circulating the cooling water in the jacket.

After reaction, the catalyst was filtrated off, and the concentration of H_2O_2 was determined on a Shimadzu UV-1800 UV−vis spectrophotometer by measuring the absorbance of the complex of Ti^{IV}-H_2O_2 [11]. A yellow complex was formed when titanium oxysulfate ($TiOSO_4$) reacts with H_2O_2 ($TiO^{2+} + H_2O_2 \rightarrow [TiO(H_2O_2)]^{2+}$). The absorbance measurement was conducted at 410 nm to colorimetrically quantify the concentration of H_2O_2 using the standard curve method. The catalysts were evaluated at least in duplicate, and the results from replicate runs agreed to within 5 %.

3. Results and discussion

3.1. Characterization of the as-prepared photocatalysts

The crystal phase of the as-synthesized CN materials was characterized by X-ray diffraction (XRD). According to Fig. 1a, *u*-CN and *ut*-CN display two diffraction peaks at 13.0 and 27.3° assignable to the (100) and (002) reflections from the intra-layer periodic ordering and the inter-layer stacking of the heptazine units, respectively [16]. The (100) peak almost disappears for *kut*-CN. For *akut*-CN, the (100) peak was positively shifted to 14.2°, and two new peaks appear at 7.6 and 9.7° indexable to the (110) and (020) reflections of PCN, respectively [12,14, 27]. Meanwhile, its (002) reflection peak is broadened. These changes signify the improved intra-layer ordering while the slightly distorted interlayer stacking for *akut*-CN [7,28].

The textural properties of the as-synthesized CN materials were investigated by N_2 physisorption. As shown in Fig. S1a, all the samples display type IV isotherms with type H3 hysteresis loop at high relative pressures, implying the existence of mesopores. As summarized in Table S1, *u*-CN has the largest specific surface area (S_{BET}) of 55 m^2 g^{-1} and pore volume (V_{pore}) of 0.18 cm^3 g^{-1}. The textural properties of *ut*-CN are similar to those of *u*-CN, but the S_{BET} and V_{pore} are slightly reduced. However, both the S_{BET} and V_{pore} of *kut*-CN are drastically dropped to 6.8 m^2 g^{-1} and 0.024 cm^3 g^{-1}, respectively. The S_{BET} and V_{pore} of *akut*-CN are recovered to 24 m^2 g^{-1} and 0.074 cm^3 g^{-1}, respectively. According to Fig. S1b, *u*-CN, *ut*-CN, and *kut*-CN display bimodal pore size distribution at ~3 nm and 30 nm and above, while *akut*-CN only displays a broad pore size distribution at ~10 nm. It is worth to mention that the S_{BET} and V_{pore} of the as-synthesized CN materials using urea as the precursor are much larger than those synthesized using melamine as
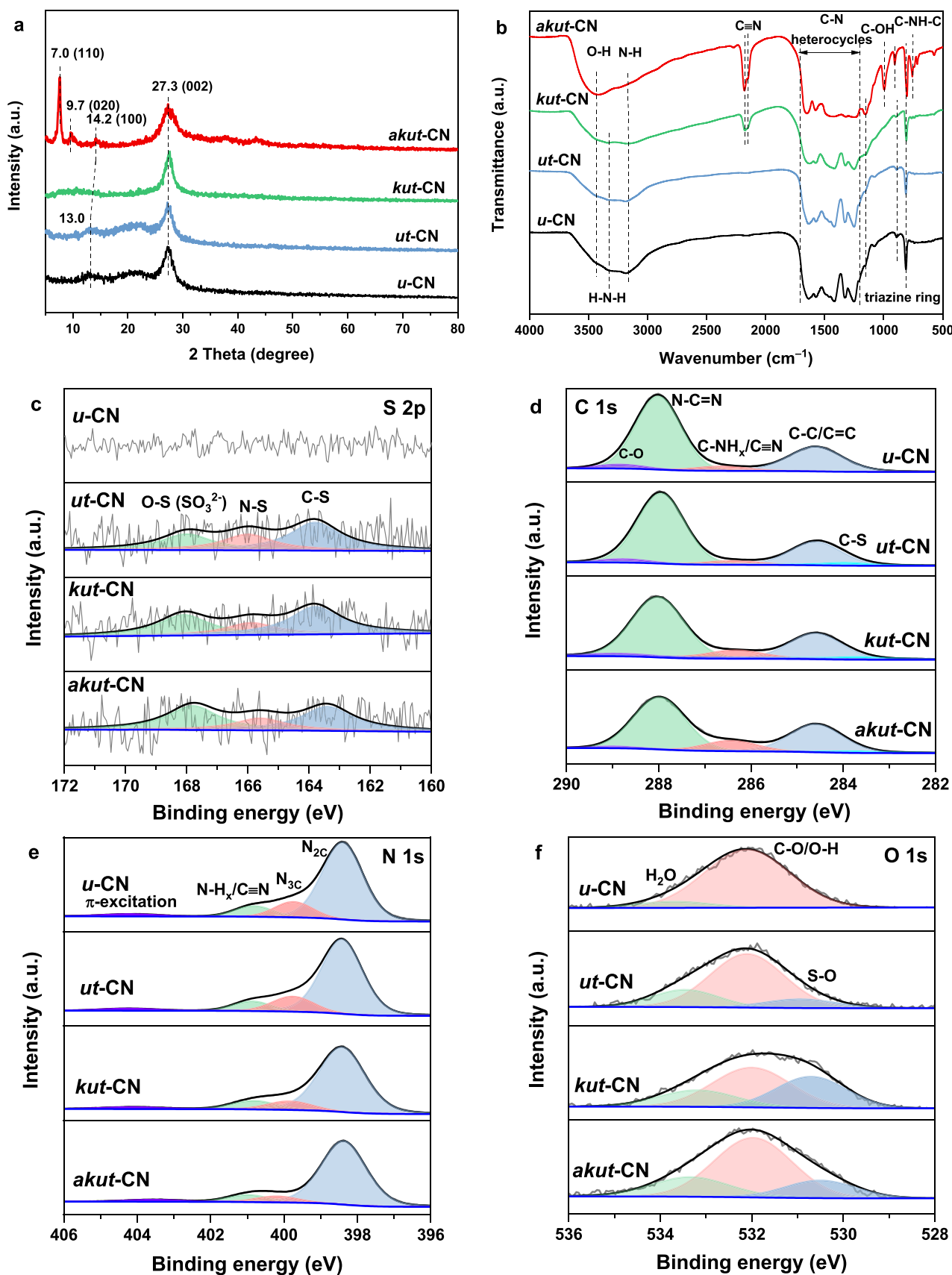
Fig. 1. (a) XRD patterns and (b) FTIR spectra of the as-synthesized CN materials. (c) S 2p, (d) C 1s, e) N 1s, and (f) O 1s spectra of the as-synthesized CN materials.

the precursor (Fig. S2 and Table S2) [7]. For example, with other precursors being identical to *akut*-CN, the S_{BET} and V_{pore} of AKMT synthesized using melamine as the precursor were only 2.4 m^2 g^{-1} and 0.01 cm^3 g^{-1}, respectively [7], which are about one order of magnitude lower than those of *akut*-CN. Therefore, *akut*-CN is expected to be favored by heterocatalysis for exposing more active sites. The higher S_{BET} and V_{pore} of *akut*-CN derived from urea can be attributed to the fact that urea is capable of releasing more gaseous products including NH$_3$, H$_2$O, and CO$_2$ [29] than melamine during thermal polymerization, which endows *akut*-CN with markedly improved porosity.

Fourier-transformed infrared (FTIR) spectroscopy was used to identify the chemical structures of the as-synthesized CN materials. In Fig. 1b, the broad bands at around 3429, 3336, and 3164 cm^{-1} are assigned to the stretching vibrations of OH, NH$_2$, and NH, respectively [30]. For *akut*-CN, the first band is intensified, while the latter two bands are attenuated. The signals in the region of 1200–1700 cm^{-1} are attributed to the stretching vibrations of the aromatic C–N heterocycles [24,27]. The band at 887 cm^{-1} is assigned to the bending vibration of the extended conjugated heptazine units [20], which is blue-shifted to 903 cm^{-1} for *akut*-CN, suggesting the disturbance of the electron structure of the PCN networks due to the doping of K and S. The sharp band at 810 cm^{-1} is assigned to the out-of-plane bending vibration of heptazine [20,27]. The slight red-shift of this band for *akut*-CN suggests the ion–dipole interaction of the heptazine units mainly with the K$^+$ ions as will be elaborated below by XPS [31,32]. These results verify that the as-synthesized CN materials retain the basic structure of heptazine despite being doped with multiple heteroatoms.

On the other hand, *kut*-CN and *akut*-CN give new bands at 2180 and 2152 cm^{-1}, which are attributed to the cyano groups (–C≡N) from the deprotonation of the terminal –C–NH$_2$ at the melon structure and the partial fracture of the heptazine unit [7,27,32], These bands are stronger on *akut*-CN than on *kut*-CN, signifying that more cyano groups are generated on the former. Furthermore, only on *akut*-CN there is a band at 997 cm^{-1} assignable to the C–OH stretching vibration, which may be related to the substitution of the terminal NH$_2$ groups on melon by the hydroxyl groups (–OH) during calcination in the presence of NaOH [7, 28,32]. The introduction of the hydroxyl groups can improve the polarity of *akut*-CN and hence enhance the hydrophilicity of the surface. The formation of the cyano and hydroxyl groups on *akut*-CN is consistent with the intensification of the O–H stretching vibration and the attenuation of the N–H$_x$ stretching vibrations. The band at 755 cm^{-1} also only visible on *akut*-CN is ascribed to the C–NH–C bending vibration [33], which may be associated with the increased intra-layer ordering of *akut*-CN as inferred by XRD.

Fig. 1c presents the S 2p spectra of the as-synthesized CN materials. On *ut*-CN, *kut*-CN, and *akut*-CN using thiourea as one of the precursors, the C–S (tertiary S, 163.8 eV) and C–S–O species (SO$_3^{2-}$, 168.1 eV) due to the substitution of the tertiary N sites and the N–S species (165.4 eV) due to the substitution of tertiary C sites in the heptazine unit are discerned [7,34]. Judging by the relative peak intensities, S is more inclined to substitute the tertiary N than the tertiary C. In the C 1s spectra (Fig. 1d), the appearance of the C–S species at 283.5 eV substantiates the S doping into the heptazine skeleton [7]. The peaks at around 289.0, 288.0, 286.3, and 284.6 eV are ascribed to the C–O, N–C≡N, C–NH$_x$ or C≡N groups, and adventitious C, respectively [27]. The noticeably enhanced peak at around 286.3 eV for *kut*-CN and *akut*-CN is attributed to the presence of more cyano groups [7,32], which is in agreement with the FTIR spectra.

In the N 1s spectra (Fig. 1e), four peaks are observed at ca. 398.4, 399.8, 400.8, and 404.0 eV, which are correlated with the C–N = C, N–(C)$_3$, N–H$_x$ or C≡N species, and π-excitation, respectively [27]. The identification of the N species in the tertiary N–(C)$_3$ and C–N = C species in conjugation with the presence of the sp^2 C species in N = C–N confirms that the as-synthesized CN materials are mainly constructed by a polymeric structure with heptazine as the basic unit [7]. Moreover, the gradual attenuation of the N–(C)$_3$ peak from *u*-CN to *akut*-CN is indicative of the gradually increased fracture degree of the heptazine units, which is consistent with the XRD and FTIR results.

According to the O 1s spectra (Fig. 1f), the peaks at 530.7, 532.0, and 533.3 eV are ascribed to the S–O, C–O [7] and/or O–H species [19,35], and adsorbed H$_2$O [35], respectively. As expected, the S–O species is absent on *u*-CN. The second peak is more intensive on *akut*-CN than on *kut*-CN, which is consistent with the FTIR result that the hydroxyl groups are generated during calcination in the presence of NaOH. Furthermore, the peak of the adsorbed H$_2$O is stronger on *ut*-CN, *kut*-CN, and *akut*-CN than on *u*-CN, demonstrating that the doping of heteroatoms can improve their surface hydrophilicity. In Fig. S3a,b, the binding energies of K 2p (K 2p$_{3/2}$ 292.5 eV) and Cl 2p (Cl 2p$_{3/2}$ 197.3 eV) of *kut*-CN and *akut*-CN are noticeably different from those of KCl with K 2p$_{3/2}$ and Cl 2p$_{3/2}$ binding energies of 293.6 and 199.2 eV, respectively [32]. In Fig. S3c, the Na 1s binding energy (1071.1 eV) of *akut*-CN also differs from that of NaOH (1072.6 eV) [31]. These results confirm the presence of the K$^+$, Cl$^-$, and Na$^+$ ions [31,32] and the strong interaction of these ions with the heptazine units. As summarized in Table S3, the surface content of K is about one to two orders of magnitude higher than those of Cl and Na, which is anticipated to dominate the ion–dipole interaction with the heptazine units. According to Ye and co-workers [20] and Choi and co-workers [7], the K$^+$ ions are inclined to coordinate with adjacent N atoms in a KN$_3$ configuration and thus bridge the adjacent layers, resulting in the K 2p$_{3/2}$ binding energy deviating from that of KCl. In addition, the results of organic element analysis and ICP-MS detected the presence of the S, K, and Na elements in *akut*-CN (Tables S4 and S5), which is in line with the XPS results.

The ^{13}C and ^{1}H solid-state magic angle spinning (MAS) nuclear magnetic resonance (NMR) spectroscopies were employed to further determine the chemical structures of the as-synthesized CN materials. In the ^{13}C NMR spectra (Fig. 2a), two prominent peaks at ~157 and ~164 ppm are ascribed to the CN$_3$ (C3) and CN$_2$–(NH$_x$) (C4) moieties in the heptazine unit [7,21,27]. The C3/C4 intensity ratio is the lowest for *akut*-CN, verifying that *akut*-CN is the most abundant in the fractured heptazine units. The inset in Fig. 2a displays the resonance peaks at ~124 ppm for –C≡N (C1), ~152 ppm for CN$_2$OH (C2), ~168 ppm for –NH–C≡N (C5), and ~172 ppm for =N–C≡N (C6) for *akut*-CN [7], confirming that the alkali-assisted calcination is conducive to the introduction of the cyano and hydroxyl groups, which is consistent with the FTIR and XPS results. The ^{1}H NMR spectra (Fig. 2b) display two main peaks at ~4.5 ppm for the –OH group and residual H$_2$O (H$_a$) and ~9.4 ppm for the –NH$_x$ groups (H$_b$) [7]. The H$_a$ peak shifts from ~4.5 ppm for *u*-CN to ~4.8 ppm for *kut*-CN and ~5.1 ppm for *akut*-CN. Moreover, this peak is the strongest for *akut*-CN, indicating the highest abundance of the hydroxyl groups and the adsorbed H$_2$O. The H$_b$ peak shifts from ~9.4 ppm for *u*-CN to ~10.3 ppm for *akut*-CN, which can be ascribed to the conversion of the –C–NH$_x$ groups to the electron-withdrawing cyano groups [7].

X-ray absorption near edge structure (XANES) was acquired to further reveal the discrepancies in the local atomic and electronic structures of *u*-CN and *akut*-CN. In the left part of the C K-edge XANES spectra (Fig. 2c), three peaks are observed at ~285.4 eV (C1), ~287.6 eV (C2), and ~288.4 eV (C3). According to Ren et al. [36], the weak C1 peak is due to the C 1s to π* (C=C) transition from the interlayer C=C bonding. This peak is barely visible for *akut*-CN, suggesting a lower degree of interlayer C=C bonding. The C2 peak is due to the C 1s to π* (C–H/C–NH$_2$) transition from the C atoms at the edge of the aromatic heptazine units. The C3 peak is the dominant XANES feature associated with the C 1s to π* (N–C=N) transition from the C atoms in the heptazine unit. The negative shift of the C3 peak of *akut*-CN may be ascribed to the existence of coordination interaction and charge transfer from pyridinic C to S. The peak at ~289.6 eV may be associated with π* (N–C) from the defect states in the PCN material, indicating the presence of more defects in *akut*-CN [36].

The N K-edge XANES spectra are shown in Fig. 2d. Three peaks are observed in the pre-edge region at 399.6 eV (N1), 401.4 eV (N2), and
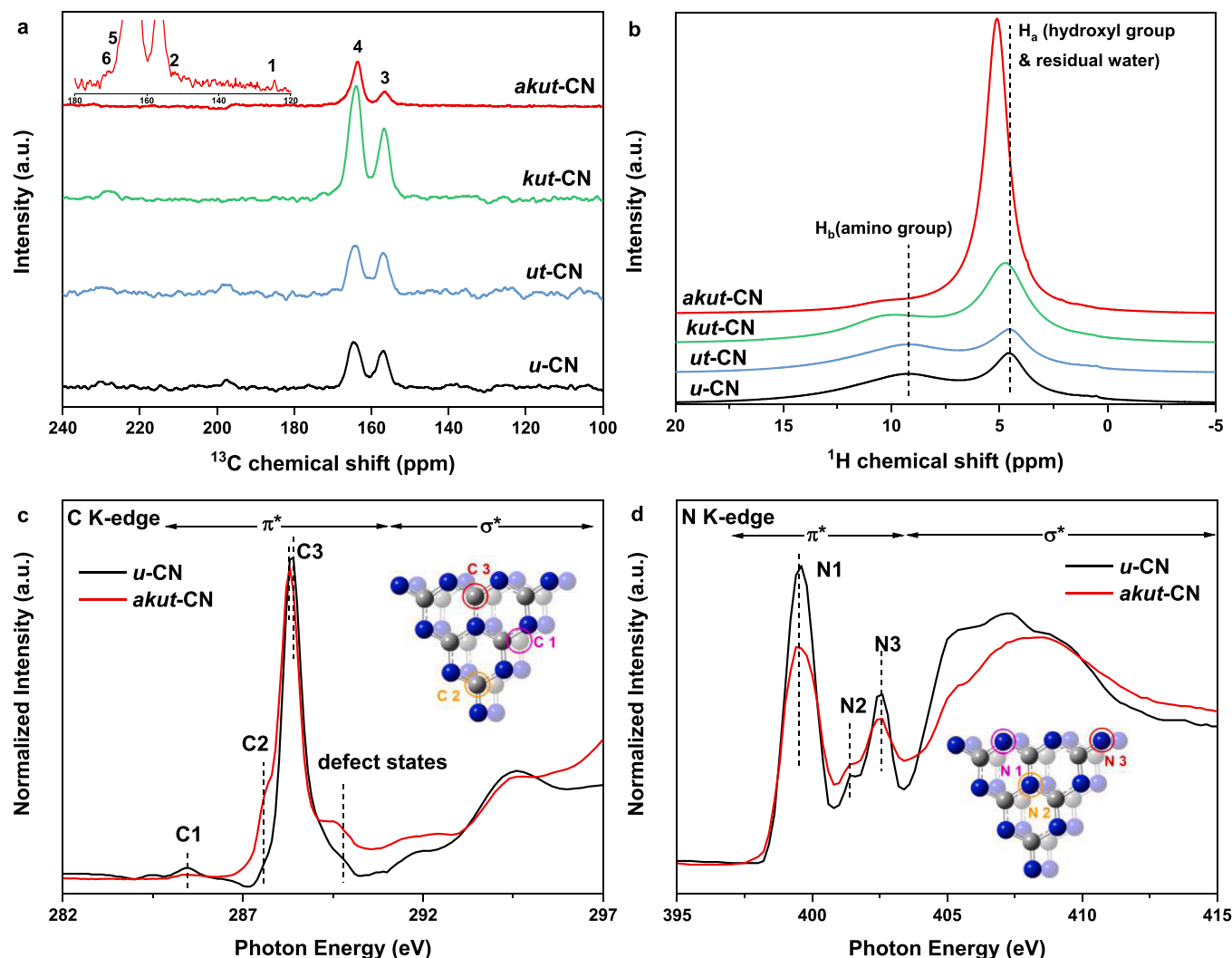
Fig. 2. (a) ^{13}C and (b) ^{1}H solid-state MAS NMR spectra of the as-synthesized CN materials. (c) C K-edge and (d) N K-edge XANES spectra of *u*-CN and *akut*-CN.

402.6 eV (N3). The N1 peak is attributed to the N 1s to π^{*} (C=N–C) transition from N atoms in the C=N–C moiety of the heptazine unit. The N2 peak is ascribed to the N 1s to π^{*} (N–(C)$_3$) transition from the graphitic N atom at the center of the heptazine unit. And the N3 peak is ascribed to the N 1s to π^{*} (N–C) transition from the sp^3 N–C that bridges three heptazine units [37]. As compared to *u*-CN, the N1 and N3 peaks of *akut*-CN are much weaker, while their N2 peaks are comparable in intensity, signifying that *akut*-CN possesses more N defects, which is consistent with the lower N/C atomic ratio determined by XPS (Table S2). In conclusion, a combination of the FTIR, XPS NMR, and XANES characterizations point to the structure of *akut*-CN as poly (heptazine-triazine imide) doped with K and S and functionalized by the cyanamide and hydroxyl groups, as depicted in Fig. S4.

The morphology of the as-synthesized CN materials was investigated by SEM and TEM. The scanning electron microscopic (SEM) images of the as-synthesized CN materials are shown as Fig. 3a–d. For *u*-CN, there are interconnected irregular particles that are composed of multilayered nanosheets. *ut*-CN possesses bended nanosheets, the enclosure of which forms the meso- and macro-pores. *kut*-CN is composed of hollow nanorods and nanoparticles with porous surfaces. *akut*-CN displays a cauliflower-like morphology formed by an aggregation of irregular nanoparticles. Transmission electron microscopy (TEM) was used to further distinguish the structural difference between *u*-CN and *akut*-CN. As shown as Fig. 3e–h, *u*-CN consists of thin nanosheets with many large meso- and macro-pores, while *akut*-CN is constructed by an aggregation

of irregular nanoparticles and nanosheets with some small mesopores. No distinct lattice fringes were discerned on the high-resolution TEM (HRTEM) image of *u*-CN. In contrast, the HRTEM image of *akut*-CN (inset in Fig. 3h) presents the lattice fringes with interplanar distances of 1.161 nm (marked in yellow) and 0.896 nm (marked in red) indexable to the (110) and (020) facets of PCN, respectively [12,14], which is in line with the XRD result that these reflections were only visible on *akut*-CN.

3.2. Photocatalytic performance in O$_2$ reduction to H$_2$O$_2$

The photocatalytic performances of the as-synthesized CN materials for O$_2$ reduction to H$_2$O$_2$ were evaluated under visible light irradiation ($\lambda > 420$ nm) if unspecified. As illustrated in Fig. 4a, when using *u*-CN as the catalyst, the H$_2$O$_2$ concentration is as low as 21.2 μM after 1 h of photoirradiation. With the increase in the proportion of thiourea, the H$_2$O$_2$ production rate increases first, reaches the maximum of 33.6 μM h^{-1} at the urea to thiourea mass ratio of 5/1 (*ut*-CN), and then decreases at higher thiourea proportions. By fixing at the optimal urea to thiourea mass ratio of 5/1, the effect of the mass ratio of KCl to the *ut*-CN precursor is shown in Fig. 4b. The H$_2$O$_2$ production rate reaches the maximum of 64.0 μM h^{-1} at the mass ratio of KCl to the *ut*-CN precursor of 1/1 (*kut*-CN). It should be mentioned that for the *kut*-CN series catalysts, the calcination temperature was lowered to 723 K, or no material was left after calcination at 823 K followed by washing. The H$_2$O$_2$
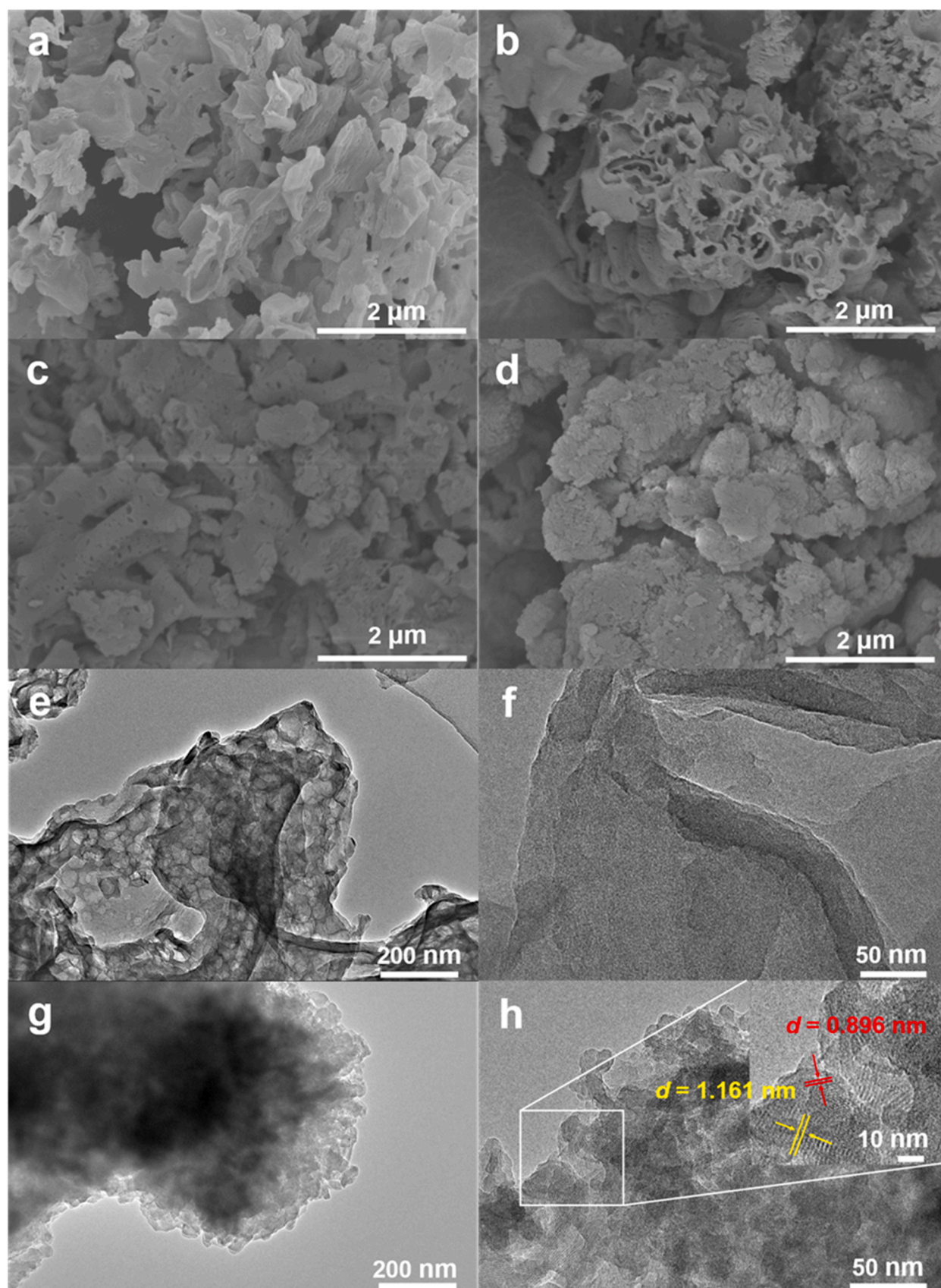
Fig. 3. SEM images of (a) *u*-CN, (b) *ut*-CN, (c) *kut*-CN, and (d) *akut*-CN, and TEM images of (e, f) *u*-CN and (g, h) *akut*-CN.
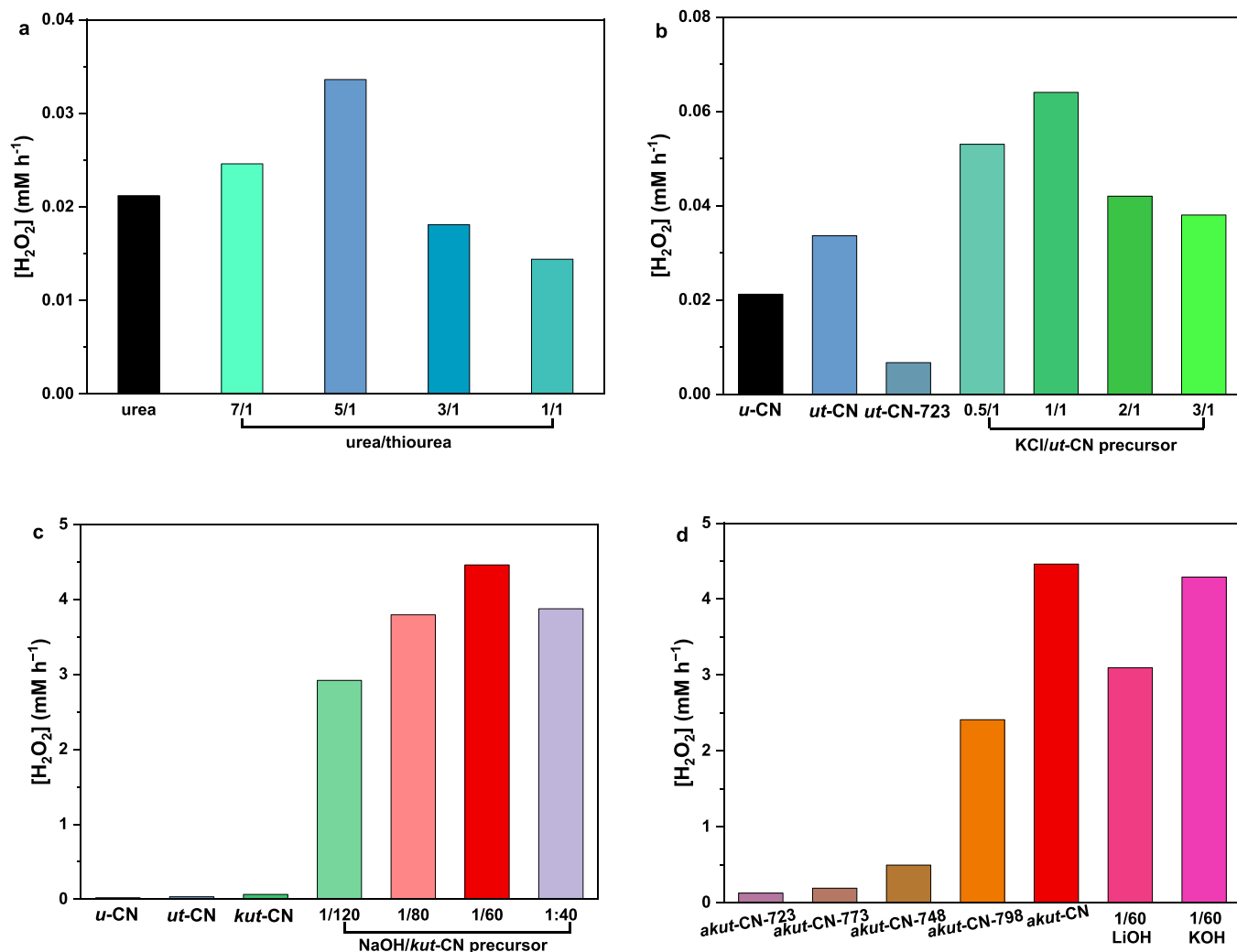
Fig. 4. Photocatalytic H_2O_2 production of as a function of the mass ratio of (a) urea to thiourea, (b) KCl to *ut*-CN precursor, c) NaOH to *kut*-CN precursor, and d) *akut*-CN-T materials, respectively. Reaction conditions: 50 mg of catalyst, 90 mL of water, 10 mL of ethanol, 1 atm of O_2, $\lambda > 420$ nm, and light intensity of ca. 150 mW cm^{-2}.

production rates over *ut*-CN and *kut*-CN are improved to about 1.6 and 3.0 times that over *u*-CN, respectively, however, their activities are in the same order of magnitude.

As illustrated in Fig. 4c, it is remarkable that only a small fraction of NaOH, that is, the mass ratio of NaOH to the *kut*-CN precursor of 1/120, drastically boosts the H_2O_2 production rate to 2.92 mM h^{-1}. The H_2O_2 production rate maximizes at 4.46 mM h^{-1} over *akut*-CN with the mass ratio of NaOH to the *kut*-CN precursor of 1/60, which is 210 times the value over *u*-CN. Moreover, a comparison with the previously reported PCN-based photocatalysts for this purpose under visible light irradiation (Table S6) reveals that *akut*-CN exhibits much better performance than other photocatalysts. In addition, the decomposition of H_2O_2 over *akut*-CN under visible light irradiation is insignificant (Fig. S5). The H_2O_2 production rates over the *akut*-CN-*T* catalysts increase monotonically with the calcination temperature from 723 to 823 K (Fig. 4d). No solid material was left at calcination temperatures higher than 823 K followed by washing. For the *akut*-CN series catalysts, the type of the base also affects the H_2O_2 production rate. As also presented in Fig. 4d, LiOH is far inferior to NaOH in enhancing the H_2O_2 production rate, while KOH is slightly less effective than NaOH. Furthermore, under UV–visible light irradiation, the H_2O_2 production rate over *akut*-CN is boosted to as high as 8.23 mM h^{-1} (Fig. S6), which is also higher than the best value reported so far over the PCN-based photocatalysts under similar reaction conditions, as compared in Table S7.

To discriminate the origin of H_2O_2 from the O_2 reduction pathway or the H_2O oxidation pathway, the reaction was additionally conducted in the air and N_2 atmospheres over *akut*-CN. Fig. 5a shows that the H_2O_2 production rates are 2.43 mM h^{-1} and 0.064 mM h^{-1} in the air and N_2 atmospheres, respectively, with 45.5 % and 98.6 % activity drops relative to that in the O_2 atmosphere. In another control experiment, we studied the photocatalytic production of H_2O_2 in pure H_2O over *akut*-CN under otherwise the same reaction conditions. As demonstrated in Fig. S7, the H_2O_2 production rate over *akut*-CN in H_2O is only 0.246 mM h^{-1}, which dramatically drops by about 94.5 % with respect to the value in the presence of ethanol. Hence, O_2 reduction rather than H_2O oxidation is the predominant pathway for H_2O_2 production over *akut*-CN. Moreover, in the blanket of a static N_2 atmosphere, no bubbles were observed in the catalyst suspension, which excludes the occurrence of the oxygen evolution reaction over *akut*-CN. Furthermore, the H_2O_2 production rate increased with the decrease in the pH value of the solution from 11 to 3 (Fig. S8), which evidences that the H_2O_2 production rate is dependent on the concentration of proton in the solution [2].

The apparent quantum yield (AQY) of photocatalytic O_2 reduction to H_2O_2 was evaluated by utilizing monochromatic light as the irradiation source (Fig. 5b). The AQY of *akut*-CN amounts to 17.2 % at 420 nm, which is ~63.7 times that of *u*-CN (0.27 %). The AQY of *akut*-CN rapidly declines at longer wavelengths, which nicely follows the UV–vis absorption profile of *akut*-CN, verifying the photocatalytic mechanism of
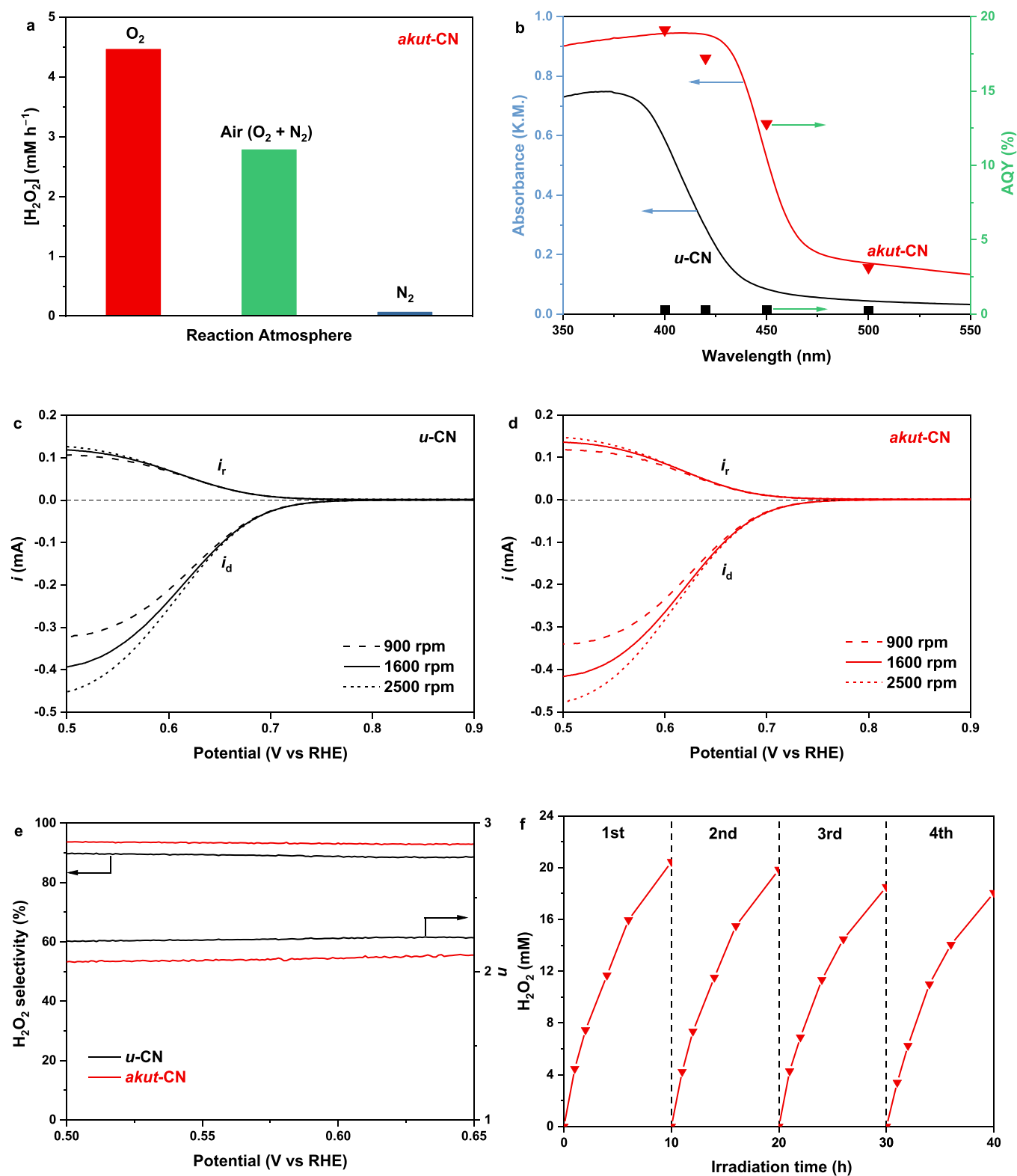
Fig. 5. (a) Effect of reaction atmosphere on the photocatalytic production rate of H_2O_2 over *akut*-CN after 1 h of visible light irradiation. (b) Apparent quantum yield (AQY) of H_2O_2 production over *u*-CN and *akut*-CN as a function of the irradiation wavelength. The linear sweep voltammetry (LSV) plots of (c) *u*-CN and (d) *akut*-CN, respectively. Reaction conditions: 50 μg of catalyst, scan rate of 10 mV s^{-1}, and O_2-saturated 0.1 M KOH electrolyte. The Pt ring was potentiostated at 1.2 V vs RHE for H_2O_2 detection. (e) The H_2O_2 selectivity over *u*-CN and *akut*-CN as a function of the applied potential at 1600 rpm and the electron transfer number. (f) Repeated runs of photocatalytic H_2O_2 production over *akut*-CN for four times under visible light irradiation.

H₂O₂ production from O₂.

As an important index pertaining to the selectivity in the 2e⁻ ORR process, the average electron transfer number (n) was estimated electrochemically on a rotating ring disc electrode (RRDE), which is a common practice in works on photocatalytic O₂ reduction to H₂O₂ [7, 15,17,19–21,25,37]. Fig. 5c,d shows the linear sweep voltammetry (LSV) curves of *u*-CN and *akut*-CN as representatives in an O₂-saturated 0.1 M KOH electrolyte. The disk current (i_d) came from the ORR reactions occurred on the catalyst-loaded disk electrode, and the ring current (i_r) came from the oxidation of H₂O₂ on the Pt ring electrode potentiostated at 1.2 V. The i_d and i_r of *akut*-CN are –0.412 and 0.134 mA at an applied voltage of 0.50 V vs RHE and a rotation speed of 1600 rpm, respectively, while *u*-CN affords lower i_d and i_r of –0.388 and 0.117 mA under the same reaction conditions, respectively. The same trend is also held when the i_d and i_r of *u*-CN and *akut*-CN are compared at 900 rpm and 2500 rpm. The H₂O₂ selectivity and average electron transfer number derived from the LSV curves obtained at 1600 rpm in Fig. 5c,d are presented in Fig. 5e. The H₂O₂ selectivity over *u*-CN is about 88 % in the potential range of 0.65–0.50 V, whereas *akut*-CN exhibits a higher H₂O₂ selectivity of around 94 % in the same potential range. The electron transfer numbers of *u*-CN and *akut*-CN are calculated to be about 2.21 and 2.13 at 0.50 V vs RHE, respectively. As displayed in Fig. S9, the electron transfer numbers of *u*-CN and *akut*-CN at 900 rpm are 2.11 and 2.06 at 0.50 V vs RHE, respectively, and the corresponding values at 2500 rpm are 2.28 and 2.18, which are also close to 2. Therefore, the O₂ reduction pathway over *u*-CN and *akut*-CN is principally 2e⁻ ORR, and *akut*-CN is more active and selective than *u*-CN in O₂ reduction to H₂O₂.

The stability of *akut*-CN in photocatalytic O₂ reduction to H₂O₂ was evaluated under visible light irradiation with the run time of each cycle being prolonged to 10 h. As shown in Fig. 5 f, the H₂O₂ concentration was 20.46 mM at the first run and gradually decreased to 18.06 mM at the fourth run. The preservation of 88 % of the initial activity after 40 h of reaction manifests the excellent stability of *akut*-CN in photocatalytic O₂ reduction to H₂O₂. The activity loss may be due to the material loss during the recovery of the powdery *akut*-CN through repetitive centrifugation and washing. The XRD pattern, FTIR spectrum, and XPS spectra of *akut*-CN after the fourth run (Fig. S10) exhibit no obvious changes as compared to those of the pristine catalyst, except for the appearance of the sulfate species with the S 2p BE of 168.1 eV) [34], which might be due to the oxidization of a fraction of the SO_3^{2-}, S–N, and C–S species by H₂O₂. These results substantiate the good stability of *akut*-CN in photocatalytic O₂ reduction to H₂O₂.
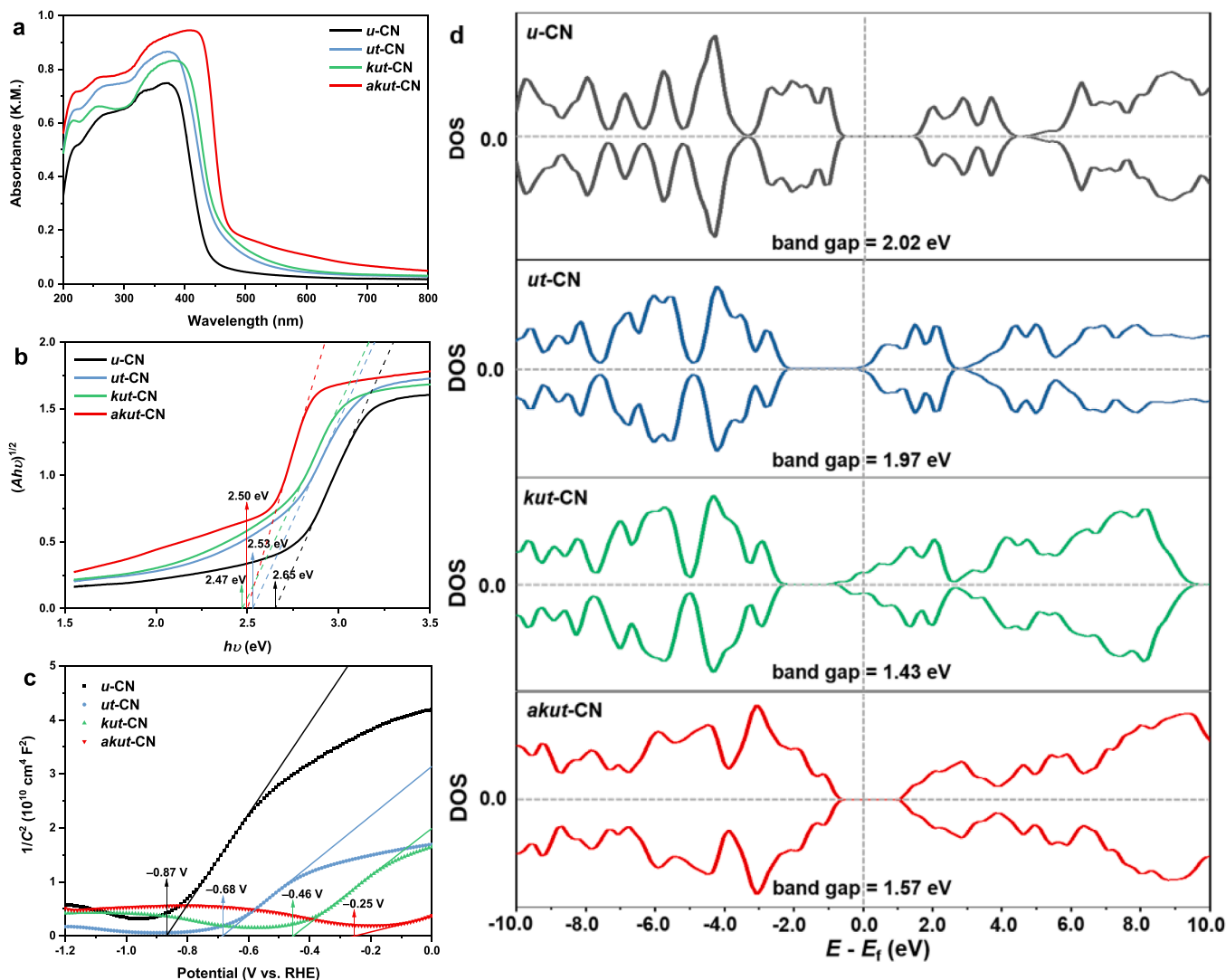

Fig. 6. (a) The UV–vis Diffuse reflectance spectra, (b) the corresponding Tauc plots, and (c) Mott–Schottky curves of the as-synsenized CN materials. (d) The calculated density of states of the as-synthesized CN materials.

3.3. Band structure

The doping of multiple heteroatoms is expected to modulate the electronic structure and band gap (E_g) of the as-synthesized CN materials. According to the UV–vis diffuse reflectance spectra (UV–vis DRS) shown in Fig. 6a, *akut*-CN displays the strongest absorption in both UV and visible light regions. The absorption edges of the as-synthesized CN materials red-shift from 440 nm for *u*-CN to 472 nm for *akut*-CN, which indicates the narrowing of the band gap. The Tauc plots show that the E_g decreases steadily from 2.65 eV for *u*-CN to 2.53 eV for *ut*-CN and to 2.47 eV for *kut*-CN, and then increases slightly to 2.50 eV for *akut*-CN (Fig. 6b).

The evolution in the band gaps of the as-synthesized CN materials was validated by the density functional theory (DFT) calculations. On the basis of the above structural characterization results and literature works [7,38], for the structural model of *ut*-CN, the S atom occupies the position of the N atom rather than the C atom in the heptazine unit (Fig. S11a,b). As for the structural model of *kut*-CN, the K^+ ion is placed in the N pot constituted by adjacent cyanamide-functionalized heptazine units and coordinated with the N atoms through the ion–dipole interaction (Fig. S11c) [39]. And for the structural model of *akut*-CN, the OH group is additionally attached to the C atom of the structure of *kut*-CN (Fig. S11d). As illustrated in Fig. 6d, the calculated band gaps are 2.02, 1.97, 1.43, and 1.57 eV for *u*-CN, *ut*-CN, *kut*-CN, and *akut*-CN, respectively, which nicely mimics the order of the band gaps derived from the Tauc plots and hence substantiates the validity of our interpretation on the structural characteristics of the as-synthesized CN materials.

The Mott–Schottky (MS) plots were used to disclose the difference in the electronic structures of the as-synthesized CN materials. In Fig. 6c, the slopes of the linear part of the $1/C^2$ vs V curves are positive, indicating that all the as-synthesized CN materials are *n*-type

semiconductors [40]. The flat band potential can be acquired from the abscissa intercept of the linear region of the $1/C^2$ vs V curve. As illustrated in Fig. 6c, the flat band potentials are –0.87, –0.68, –0.46, and –0.25 eV for *u*-CN, *ut*-CN, *kut*-CN, and *akut*-CN, respectively. Since the conduction band (CB) bottom of the *n*-type semiconductor is commonly considered to be about 0.1–0.2 eV negative to the flat band potential [21], when taking the potential discrepancy as 0.1 eV, the CB bottom potentials of *u*-CN, *ut*-CN, *kut*-CN, and *akut*-CN are estimated to be –0.97, –0.78, –0.56, and –0.35 eV, respectively, which are all capable of reducing O_2 to H_2O_2. Coupling with their band gaps, the valence band (VB) top potentials of *u*-CN, *ut*-CN, *kut*-CN, and *akut*-CN are estimated to be 1.68, 1.74, 1.94, and 2.15 eV, respectively, which is consistent with previous findings that the cyano group can simultaneously lower the CB and VB levels of PCN [41]. Fig. S12 illustrates the band energy structures of the as-synthesized CN materials.

3.4. The mechanism of akut-CN in photocatalytic H₂O₂ production

From the MS plots in Fig. 6c, the electron donor concentrations are estimated to be 3.05×10^{20}, 5.61×10^{20}, 5.85×10^{20}, and 1.81×10^{21} cm^{-3} for *u*-CN, *ut*-CN, *kut*-CN, and *akut*-CN, respectively, on the basis of the slopes of the linear region of 8.42×10^{10}, 4.58×10^{10}, 4.39×10^{10}, and 1.41×10^{10}, respectively [40]. The highest electron donor concentration of *akut*-CN is consistent with its highest contents of the alkali heteroatoms that can donate electrons to the PCN framework.

The photogenerated electron–hole pair separation was characterized by the steady-state photoluminescence emission (PL) spectroscopy and time-resolved photoluminescence (TR-PL) spectroscopy. In Fig. 7a, *u*-CN displays the strongest PL peak at around 450 nm. The PL intensity markedly weakens in the order of *u*-CN > *ut*-CN > *kut*-CN > *akut*-CN, demonstrating that the separation efficiency of the photogenerated
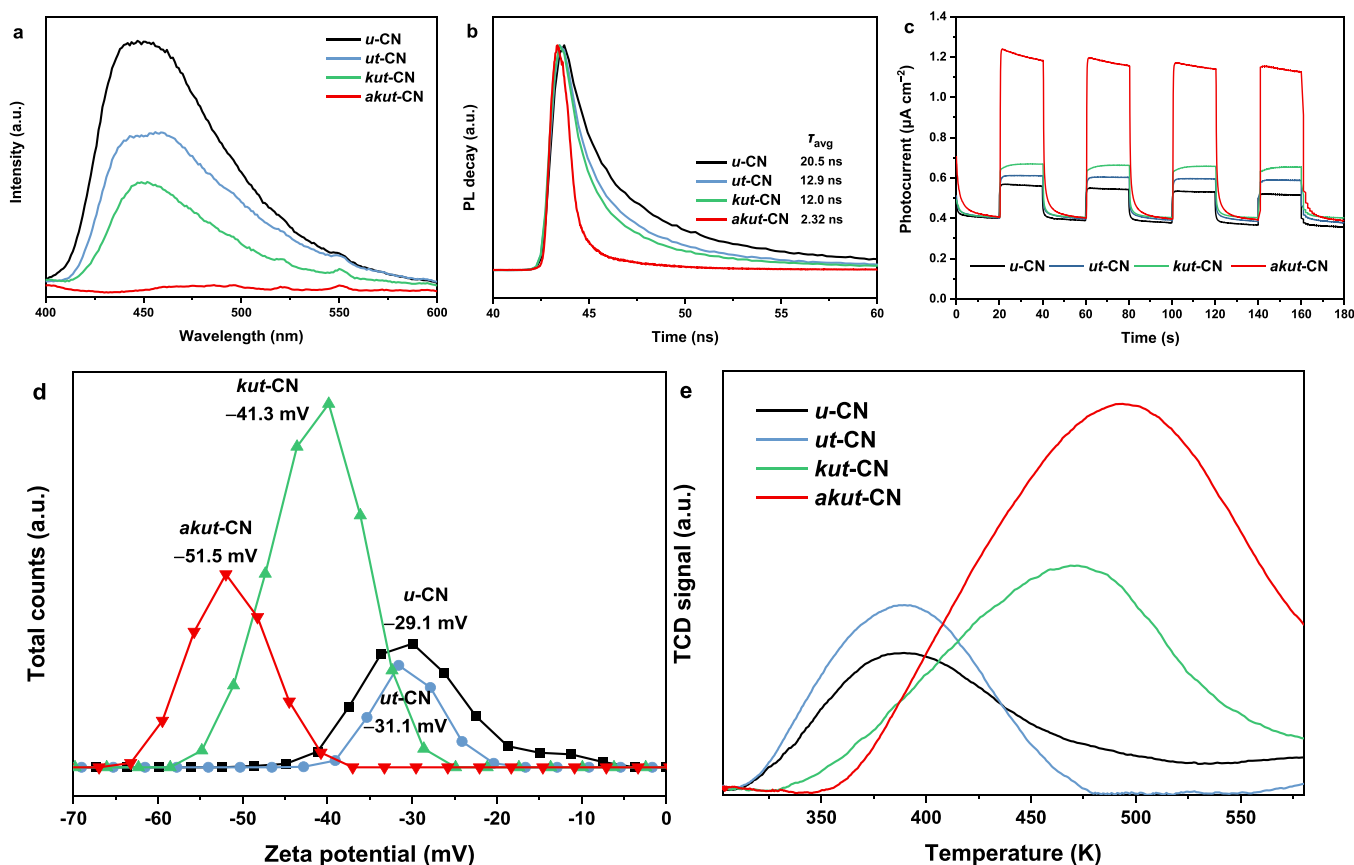

Fig. 7. (a) Steady-state photoluminescence spectra, (b) time-resolved fluorescence decay spectra, (c) photocurrent response curves, d) Zeta potentials, and (e) O₂-TPD profiles of the as-synthesized CN materials.

electron–hole pair is the highest on *akut*-CN. The TR-PL spectroscopy was used to analyze the decay kinetics of the electron–hole pairs. As shown in Fig. 7b and summarized in Table S8, the average lifetimes (τ_{avg}) of the photogenerated charge carriers are 20.5, 12.9, 12.1, and 2.32 ns for *u*-CN, *ut*-CN, *kut*-CN, and *akut*-CN, respectively, demonstrating the fastest decay kinetics of the electron–hole pairs for *akut*-CN. The weakest PL emission intensity and the shortest τ_{avg} reflect the most reduced electron–hole recombination and the lowest population of the survived photoinduced electron–hole pairs due to the fastest charge separation on *akut*-CN [42].

The photocurrent response measurement was utilized to investigate the charge separation and transportation behavior. As shown in Fig. 7c, all the catalysts display immediate response upon light on/off cycles, manifesting efficient generation and interface transfer of the photogenerated charge carriers. The photocurrent intensity increases in the order of *u*-CN < *ut*-CN < *kut*-CN < *akut*-CN, indicating the highest concentration and the most efficient separation and interface transfer of the photogenerated charge carriers on *akut*-CN, which is compatible with the MS, PL, and TR-PL results.

For *akut*-CN, the E_g is larger than that of *kut*-CN, the CB bottom is the least negative among the as-synthesized CN materials, and the S_{BET} is lower than those of *u*-CN and *ut*-CN (Table S1). However, *akut*-CN exhibited the highest H$_2$O$_2$ production rate among the as-synthesized CN materials, indicating that the thermodynamic driving force and the surface area are not the main factors that determine the photocatalytic activity of O$_2$ reduction to H$_2$O$_2$ in the present case. On the other hand, it is acknowledged that the concentration of the electron donor and the separation and recombination of the photogenerated charge carriers pronouncedly influence the catalytic efficiency [40]. The MS (Fig. 6c) and photocurrent response characterizations (Fig. 7c) revealed that both the electron donor concentration and photocurrent intensity increase in the order of *u*-CN < *ut*-CN < *kut*-CN < *akut*-CN. The PL (Fig. 7a) and TR-PL characterizations (Fig. 7b) disclosed that both the PL intensity and the lifetime of the electron–hole pairs decreased in the order of *u*-CN > *ut*-CN > *kut*-CN > *akut*-CN. Coherently, the H$_2$O$_2$ production rate increases in the order of *u*-CN < *ut*-CN < *kut*-CN < *akut*-CN, suggesting that the concentration and the efficiencies in the separation and interface transfer of the photogenerated charge carriers are responsible for the photocatalytic performances of the as-synthesized CN materials in O$_2$ reduction to H$_2$O$_2$. It was reported that the K$^+$ ions in the N pots can drastically rearrange the charge distribution between the neighboring conjugated heptazine planes, which greatly enhances the electronic coupling between the alkali metal cation-bridged layers and hence facilitates the interlayer charge transfer and separation [7,43].

On the other hand, since the photocatalytic O$_2$ reduction to H$_2$O$_2$ proceeds via the proton-coupled two-electron reduction mechanism [7,19,38], as also verified by the pH-dependent H$_2$O$_2$ production rate (Fig. S8) and RRDE measurements (Fig. 5c–e), in addition to the availability of the photoinduced electrons, the protons and O$_2$ are indispensable to the occurrence of the reaction. The FTIR, XPS NMR, and XANES characterizations (Fig. 1 and Fig. 2) revealed that when calcinating urea and thiourea in the presence of KCl, the cyano groups are generated at the expense of the –C–NH$_x$ groups. The adding of NaOH during calcination further increases the amount of the cyano groups and incorporates the hydroxyl groups to the heptazine skeleton by replacing the amino groups. The introduction of these functional groups is expected to affect the surface polarity and the adsorption behavior of O$_2$ on PCN. As shown in Fig. 7d, the as-synthesized CN materials are more and more negatively charged in distilled water, with the Zeta potentials ranking in the order of −29.1 mV (*u*-CN) < −31.1 mV (*ut*-CN) < −41.3 mV (*kut*-CN) < −51.5 mV (*akut*-CN). The more negatively charged surface is anticipated to be easier for the protons to adsorb and accumulate on the catalyst surface via the electrostatic attraction [32], which is beneficial to the proton-coupled photocatalytic reduction of O$_2$ to H$_2$O$_2$ [7].

The control experiments have demonstrated that the H$_2$O$_2$

productivity is closely related to the concentration of O$_2$ (Fig. 5a). Xin et al. found that O$_2$ adsorption was enhanced by the hydroxyl groups on the coal surface [44]. By reacting formaldehyde with the amino groups on g-C$_3$N$_4$, He and co-workers introduced hydroxyl groups on g-C$_3$N$_4$ synthesized from melamine, which exhibited over 12.8 times the activity of the pristine g-C$_3$N$_4$ in H$_2$O$_2$ production. By excluding the effects of the hydroxyl groups on the morphology, light absorption intensity and edge, band positions, and charge separation and transfer properties in that case, the authors concluded that the hydroxyl groups on the modified g-C$_3$N$_4$ improved O$_2$ adsorption capacity and kinetically promoted the protonation steps of the adsorbed O$_2$ [19], which are generally considered as the rate-limiting steps [38]. Ao and co-workers found that on the fragmented and ultrathin TP-PCN, the cyano and hydroxyl groups greatly enhanced the adsorption capacity and binding strength of O$_2$ and reduced the energy barrier of H$_2$O$_2$ formation [37]. Therefore, the adsorption behavior of O$_2$ on the as-synthesized CN materials was investigated by temperature-programmed desorption of O$_2$ (O$_2$-TPD). The area under the O$_2$ desorption peak represents the amount of O$_2$ trapped by the catalyst, whereas the desorption temperature reflects the binding strength of O$_2$ on the catalyst surface. According to Fig. 7e, the desorption peaks of *kut*-CN and *akut*-CN are much stronger than those of *u*-CN and *ut*-CN. The O$_2$ desorption temperatures on *kut*-CN and *akut*-CN are also much higher than those on *u*-CN and *ut*-CN, indicating that *kut*-CN and *akut*-CN had much stronger binding strength towards O$_2$. In particular, *akut*-CN displays the largest desorption peak and the highest desorption temperature of O$_2$. The enhanced adsorption capacity and strength of O$_2$ on *kut*-CN can be ascribed to the presence of the cyano groups. Since *akut*-CN is the most abundant in the cyano and hydroxyl groups, it displays the largest adsorption capacity and the highest binding strength of O$_2$, thus further elevating the activity in photocatalytic O$_2$ reduction. The DFT calculations of Ao and co-workers disclosed that the cyano and hydroxyl groups can pronouncedly promote direct electron transfer from the β spin-orbital in TP-PCN to the π * orbital of O$_2$, which leads to more negative adsorption energy (E_{ads}) of O$_2$ than other locations [37]. On the basis of the above discussion, the plausible mechanism for the highly efficient photocatalytic O$_2$ reduction to H$_2$O$_2$ over *akut*-CN is proposed, as illustrated in Scheme 1.

Finally, it should be mentioned that like many literature works, the photocatalytic activities of the as-synthesized CN materials reported here did not involve the rate of photon absorption in the reactor that varies with catalyst concentration and with catalyst specimens. For a more rigorous comparison of the photocatalytic activity, the catalyst optical parameters (absorption and scattering coefficients in the aqueous suspension), reactor optical thickness, and total rate of photon
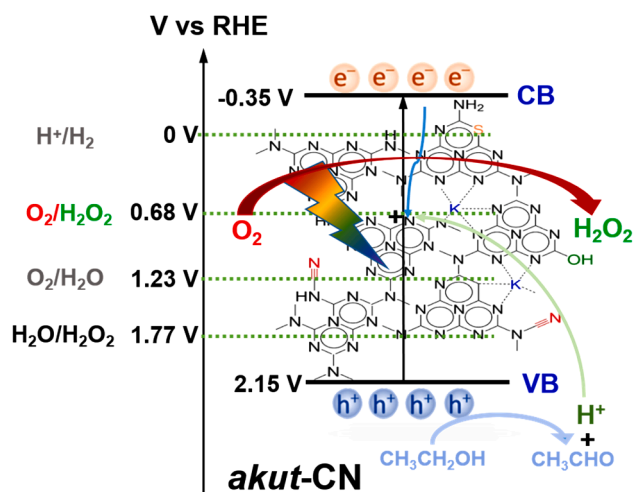
Scheme 1. Plausible reaction mechanism for the selective photoproduction of H$_2$O$_2$ over *akut*-CN via the proton-couple two-electron O$_2$ reduction route.

absorption should be evaluated, and photocatalytic reactors such as annular reactor and flat reactor that are operated in the steady-state and continuous manner with the laminar flow should be adopted rather than the current batch-wise stirred reactor with the turbulent flow so as to simplify the modelling of radiation emission/incidence, radiation absorption–scattering, kinetics, and fluid-dynamics as well as the mathematical treatment of these models [45–47].

4. Conclusion

By one-pot polymerization of urea and thiourea in the presence of KCl and NaOH, we have successfully fabricated a highly active, selective, and stable multiple heteroatom-doped *akut*-CN for photocatalytic O_2 reduction to H_2O_2. The excellent catalytic performance of *akut*-CN is mainly attributed to the high concentration and efficient separation and transfer of the photoinduced charge carriers, and the highly negatively charged surface and the enhanced O_2 adsorption capacity and binding strength, which kinetically accelerates H_2O_2 production via the proton-coupled two-electron O_2 reduction route. This facile and effective synthetic strategy is expected to inspire more attempts to improve the processes of generation and transmission of the photoinduced charge carriers and optimize the surface properties of PCN to advance the practical application of the photocatalytic O_2 reduction to H_2O_2 process that is cost-effective, clean, and safe.

CRediT authorship contribution statement

Sitan Li: Conceptualization, Methodology, Investigation, Formal analysis, Data curation, Writing – original draft. **Bo Feng:** Conceptualization, Investigation. **Xiaoxin Zhang:** Formal analysis, Writing – review & editing. **Jing Tian:** Formal analysis. **Dan Wang:** Investigation. **Yan Pei:** Formal analysis. **Minghua Qiao:** Supervision, Funding acquisition, Formal analysis, Writing - review & editing. **Yefei Li:** Investigation. **Baoning Zong:** Supervision, Funding acquisition.

Declaration of Competing Interest

The authors declare that they have no known competing financial interests or personal relationships that could have appeared to influence the work reported in this paper.

Data Availability

Data will be made available on request.

Acknowledgements

Appendix A. Supporting information

Supplementary data associated with this article can be found in the online version at doi:10.1016/j.apcatb.2023.122879.

References

[1] Y.Y. Sun, L. Han, P. Strasser, A comparative perspective of electrochemical and photochemical approaches for catalytic H_2O_2 production, Chem. Soc. Rev. 49 (2020) 6605–6631.

[2] H.L. Hou, X.K. Zeng, X.W. Zhang, Production of hydrogen peroxide by photocatalytic processes, Angew. Chem. Int. Ed. 59 (2020) 17356–17376.

[3] J.H. Lunsford, The direct formation of H_2O_2 from H_2 and O_2 over palladium catalysts, J. Catal. 216 (2003) 455–460.

[4] G. Blanco-Brieva, E. Cano-Serrano, J.M. Campos-Martin, J.L.G. Fierro, Direct synthesis of hydrogen peroxide solution with palladium-loaded sulfonic acid polystyrene resins, Chem. Commun. (2004) 1184–1185.

[5] J.M. Campos-Martin, G. Blanco-Brieva, J.L.G. Fierro, Hydrogen peroxide synthesis: An outlook beyond the anthraquinone process, Angew. Chem. Int. Ed. 45 (2006) 6962–6984.

[6] J.K. Edwards, B. Solsona, E.N. N, A.F. Carley, A.A. Herzing, C.J. Kiely, G. J. Hutchings, Switching off hydrogen peroxide hydrogenation in the direct synthesis process, Science 323 (2009) 1037–1041.

[7] P. Zhang, Y.W. Tong, Y. Liu, J.J.M. Vequizo, H.W. Sun, C. Yang, A. Yamakata, F. T. Fan, W. Lin, X.C. Wang, W. Choi, Heteroatom dopants promote two-electron O_2 reduction for photocatalytic production of H_2O_2 on polymeric carbon nitride, Angew. Chem. Int. Ed. 59 (2020) 16209–16217.

[8] W.J. Ong, L.L. Tan, Y.H. Ng, S.T. Yong, S.P. Chai, Graphitic Carbon Nitride (g-C_3N_4)-based photocatalysts for artificial photosynthesis and environmental remediation: are we a step closer to achieving sustainability? Chem. Rev. 116 (2016) 7159–7329.

[9] S.W. Cao, J.X. Low, J.G. Yu, M. Jaroniec, Polymeric photocatalysts based on graphitic carbon nitride, Adv. Mater. 27 (2015) 2150–2176.

[10] G.F. Liao, Y. Gong, L. Zhang, H. Gao, G.J. Yang, B.Z. Fang, Semiconductor polymeric graphitic carbon nitride photocatalysts: the "holy grail" for the photocatalytic hydrogen evolution reaction under visible light, Energy Environ. Sci. 12 (2019) 2080–2147.

[11] H.H. Ou, C. Tang, X.R. Chen, M. Zhou, X.C. Wang, Solvated electrons for photochemistry syntheses using conjugated carbon nitride polymers, ACS Catal. 9 (2019) 2949–2955.

[12] Y.S. Xu, X. He, H. Zhong, D.J. Singh, L.J. Zhang, R.H. Wang, Solid salt confinement effect: An effective strategy to fabricate high crystalline polymer carbon nitride for enhanced photocatalytic hydrogen evolution, Appl. Catal. B 246 (2019) 349–355.

[13] G.G. Zhang, L.H. Lin, G.S. Li, Y.F. Zhang, A. Savateev, S. Zafeiratos, X.C. Wang, M. Antonietti, Ionothermal synthesis of triazine-heptazine-based copolymers with apparent quantum yields of 60 % at 420 nm for solar hydrogen production from "sea water", Angew. Chem. Int. Ed. 57 (2018) 9372–9376.

[14] Y.S. Xu, C.T. Qiu, X. Fan, Y.H. Xiao, G.Q. Zhang, K.Y. Yu, H.X. Ju, X. Ling, Y.F. Zhu, C.L. Su, K^+-induced crystallization of polymeric carbon nitride to boost its photocatalytic activity for H_2 evolution and hydrogenation of alkenes, Appl. Catal. B 268 (2020), 118457.

[15] Y. Shiraishi, Y. Kofuji, H. Sakamoto, S. Tanaka, S. Ichikawa, T. Hirai, Effects of surface defects on photocatalytic H_2O_2 production by mesoporous graphitic carbon nitride under visible light irradiation, ACS Catal. 5 (2015) 3058–3066.

[16] G.H. Moon, M. Fujitsuka, S. Kim, T. Majima, X. Wang, W. Choi, Eco-friendly photochemical production of H_2O_2 through O_2 reduction over carbon nitride frameworks incorporated with multiple heteroelements, ACS Catal. 7 (2017) 2886–2895.

[17] S. Kim, G.-h Moon, H. Kim, Y. Mun, P. Zhang, J. Lee, W. Choi, Selective charge transfer to dioxygen on KPF_6-modified carbon nitride for photocatalytic synthesis of H_2O_2 under visible light, J. Catal. 357 (2018) 51–58.

[18] L. Zhou, J.Y. Lei, F.C. Wang, L.Z. Wang, M.R. Hoffmann, Y.D. Liu, S.-I. In, J. L. Zhang, Carbon nitride nanotubes with in situ grafted hydroxyl groups for highly efficient spontaneous H_2O_2 production, Appl. Catal. B 288 (2021), 119993.

[19] B.Y. Liu, J.Y. Du, G.L. Ke, B. Jia, Y.J. Huang, H.C. He, Y. Zhou, Z.G. Zou, Boosting O_2 reduction and H_2O dehydrogenation kinetics: surface N-hydroxymethylation of g-C_3N_4 photocatalysts for the efficient production of H_2O_2, Adv. Funct. Mater. 32 (2021) 2111125.

[20] Y. Xie, Y.X. Li, Z.H. Huang, J.Y. Zhang, X.F. Jia, X.-S. Wang, J.H. Ye, Two types of cooperative nitrogen vacancies in polymeric carbon nitride for efficient solar-driven H_2O_2 evolution, Appl. Catal. B 265 (2020), 118581.

[21] Z. Wei, M.L. Liu, Z.J. Zhang, W.Q. Yao, H.W. Tan, Y.F. Zhu, Efficient visible-light-driven selective oxygen reduction to hydrogen peroxide by oxygen-enriched graphitic carbon nitride polymers, Energy Environ. Sci. 11 (2018) 2581–2589.

[22] L.P. Yang, G.H. Dong, D.L. Jacobs, Y.H. Wang, L. Zang, C.Y. Wang, Two-channel photocatalytic production of H_2O_2 over g-C_3N_4 nanosheets modified with perylene imides, J. Catal. 352 (2017) 274–281.

[23] S. Zhao, T. Guo, X. Li, T. Xu, B. Yang, X. Zhao, Carbon nanotubes covalent combined with graphitic carbon nitride for photocatalytic hydrogen peroxide production under visible light, Appl. Catal. B 224 (2018) 725–732.

[24] Y. Kofuji, S. Ohkita, Y. Shiraishi, H. Sakamoto, S. Tanaka, S. Ichikawa, T. Hirai, Graphitic carbon nitride doped with biphenyl diimide: efficient photocatalyst for hydrogen peroxide production from water and molecular oxygen by sunlight, ACS Catal. 6 (2016) 7021–7029.

[25] H.-i Kim, Y. Choi, S. Hu, W. Choi, J.-H. Kim, Photocatalytic hydrogen peroxide production by anthraquinone-augmented polymeric carbon nitride, Appl. Catal. B 229 (2018) 121–129.

[26] J.S. Cai, J.Y. Huang, S.C. Wang, J. Iocozzia, Z.T. Sun, J.Y. Sun, Y.K. Yang, Y.K. Lai, Z.Q. Lin, Crafting mussel-inspired metal nanoparticle-decorated ultrathin graphitic carbon nitride for the degradation of chemical pollutants and production of chemical resources, Adv. Mater. 31 (2019) 1806314.

[27] G.Q. Zhang, Y.S. Xu, D.F. Yan, C.X. He, Y.L. Li, X.Z. Ren, P.X. Zhang, H.W. Mi, Construction of K^+ ion gradient in crystalline carbon nitride to accelerate exciton dissociation and charge separation for visible light H_2 production, ACS Catal. 11 (2021) 6995–7005.

[28] Y.X. Li, S.X. Ouyang, H. Xu, X. Wang, Y.P. Bi, Y.F. Zhang, J.H. Ye, Constructing solid-gas-interfacial fenton reaction over alkalinized-C$_3$N$_4$ photocatalyst to achieve apparent quantum yield of 49 % at 420 nm, J. Am. Chem. Soc. 138 (2016) 13289–13297.

[29] J.H. Liu, T.K. Zhang, Z.C. Wang, G. Dawson, W. Chen, Simple pyrolysis of urea into graphitic carbon nitride with recyclable adsorption and photocatalytic activity, J. Mater. Chem. 21 (2011) 14398–14401.

[30] J. Yang, Y.J. Liang, K. Li, G. Yang, K. Wang, R. Xu, X.J. Xie, One-step synthesis of novel K$^+$ and cyano groups decorated triazine-/heptazine-based g-C$_3$N$_4$ tubular homojunctions for boosting photocatalytic H$_2$ evolution, Appl. Catal. B 262 (2020), 118252.

[31] W.J. Fang, J.Y. Liu, L. Yu, Z. Jiang, W.F. Shangguan, Novel (Na, O) co-doped g-C$_3$N$_4$ with simultaneously enhanced absorption and narrowed bandgap for highly efficient hydrogen evolution, Appl. Catal. B 209 (2017) 631–636.

[32] P. Zhang, D.R. Sun, A. Cho, S. Weon, S. Lee, J. Lee, J.W. Han, D.P. Kim, W. Choi, Modified carbon nitride nanozyme as bifunctional glucose oxidase-peroxidase for metal-free bioinspired cascade photocatalysis, Nat. Commun. 10 (2019) 940.

[33] M.K. Bhunia, K. Yamauchi, K. Takanabe, Harvesting solar light with crystalline carbon nitrides for efficient photocatalytic hydrogen evolution, Angew. Chem. Int. Ed. 53 (2014) 11001–11005.

[34] W. Cha, I.Y. Kim, J.M. Lee, S. Kim, K. Ramadass, K. Gopalakrishnan, S. Premkumar, S. Umapathy, A. Vinu, Sulfur-doped mesoporous carbon nitride with an ordered porous structure for sodium-ion batteries, ACS Appl. Mater. Interfaces 11 (2019) 27192–27199.

[35] Y. Zhu, L. Tian, Z. Jiang, Y. Pei, S.H. Xie, M.H. Qiao, K.N. Fan, Heteroepitaxial growth of gold on flowerlike magnetite: an efficacious and magnetically recyclable catalyst for chemoselective hydrogenation of crotonaldehyde to crotyl alcohol, J. Catal. 281 (2011) 106–118.

[36] J. Ren, L. Lin, K. Lieutenant, C. Schulz, D. Wong, T. Gimm, A. Bande, X. Wang, T. Petit, Role of dopants on the local electronic structure of polymeric carbon nitride photocatalysts, Small Methods 5 (2021), e2000707.

[37] H.N. Che, X. Gao, J. Chen, J. Hou, Y.H. Ao, P.F. Wang, Iodide-induced fragmentation of polymerized hydrophilic carbon nitride for high-performance quasi-homogeneous photocatalytic H$_2$O$_2$ production, Angew. Chem. Int. Ed. 60 (2021) 25546–25550.

[38] Y.W. Tong, C.G. Wei, Y. Li, Y.F. Zhang, W. Lin, Unraveling the mechanisms of S-doped carbon nitride for photocatalytic oxygen reduction to H$_2$O$_2$, Phys. Chem. Chem. Phys. 22 (2020) 21099–21107.

[39] H.L. Gao, S.C. Yan, J.J. Wang, Z.G. Zou, Ion coordination significantly enhances the photocatalytic activity of graphitic-phase carbon nitride, Dalton Trans. 43 (2014) 8178–8183.

[40] Z.F. Hu, Z.R. Shen, J.C. Yu, Converting carbohydrates to carbon-based photocatalysts for environmental treatment, Environ. Sci. Technol. 51 (2017) 7076–7083.

[41] H.J. Yu, R. Shi, Y.X. Zhao, T. Bian, Y.F. Zhao, C. Zhou, G.I.N. Waterhouse, L.Z. Wu, C.H. Tung, T.R. Zhang, Alkali-assisted synthesis of nitrogen deficient graphitic carbon nitride with tunable band structures for efficient visible-light-driven hydrogen evolution, Adv. Mater. 29 (2017) 1605148..

[42] Z.X. Zeng, X. Quan, H.T. Yu, S. Chen, Y.B. Zhang, H.M. Zhao, S.S. Zhang, Carbon nitride with electron storage property: enhanced exciton dissociation for high-efficient photocatalysis, Appl. Catal. B 236 (2018) 99–106.

[43] T. Xiong, W.L. Cen, Y.X. Zhang, F. Dong, Bridging the g-C$_3$N$_4$ interlayers for enhanced photocatalysis, ACS Catal. 6 (2016) 2462–2472.

[44] H.H. Xin, D.M. Wang, G.L. Dou, X.Y. Qi, T. Xu, G.S. Qi, The infrared characterization and mechanism of oxygen adsorption in coal, Spectrosc. Lett. 47 (2014) 664–675.

[45] G. Li Puma, A. Brucato, Dimensionless analysis of slurry photocatalytic reactors using two-flux and six-flux radiation absorption–scattering models, Catal. Today 122 (2007) 78–90.

[46] I. Grčić, G. Li Puma, Six-flux absorption-scattering models for photocatalysis under wide-spectrum irradiation sources in annular and flat reactors using catalysts with different optical properties, Appl. Catal. B 211 (2017) 222–234.

[47] R. Acosta-Herazo, M.Á. Mueses, G. Li Puma, F. Machuca-Martínez, Impact of photocatalyst optical properties on the efficiency of solar photocatalytic reactors rationalized by the concepts of initial rate of photon absorption (IRPA) dimensionless boundary layer of photon absorption and apparent optical thickness, Chem. Eng. J. 356 (2019) 839–849.